Inorganic Chemistry

Article

pubs.acs.org/IC

Crystallographic, Electronic, and Magnetic Properties of Rock Salt Superstructure Sulfide Lu_2CrS_4 with Jahn–Teller Distortion

Keitaro Tezuka,*[,†] Makoto Wakeshima,[‡] Masataka Nozawa,[†] Keita Oshikane,[†] Kenji Ohoyama,[§] Yue Jin Shan,[†] Hideo Imoto,[†] and Yukio Hinatsu[‡]

[†]Research Division of Functional Materials Design, Graduate School of Engineering, Utsunomiya University, Utsunomiya 321-8585, Japan

[‡]Division of Chemistry, Graduate School of Science, Hokkaido University, Sapporo 060-0810, Japan

[§]Institute of Materials Research, Tohoku University, Sendai 980-8577, Japan

Supporting Information

ABSTRACT: A new chromium(II) sulfide, Lu_2CrS_4, with a novel structure was prepared by a solid-state reaction. The powder X-ray diffraction pattern could be indexed as a tetragonal system, with a = 7.46373(2) Å, c = 22.6338(2) Å, and space group $I\bar{4}2d$ (No. 122). Rietveld analysis of the pattern provided the crystal structure consisting of CrS_6 and LuS_6 octahedra sharing edges and apexes and revealed a rock salt superstructure with new cation (vacancy) arrangements. The electrical resistivity indicates semiconducting behavior. The magnetic susceptibility and specific heat measurements showed that the Cr ions are in the high-spin d^4 configuration and that their magnetic moments ordered antiferromagnetically at 55 K. The basic antiferromagnetic structure was determined using powder neutron diffraction data at 10 K. The band structure calculations demonstrate that the densities of states of Cr 3d electrons split into two spin-up e_g bands because of Jahn–Teller distortion.

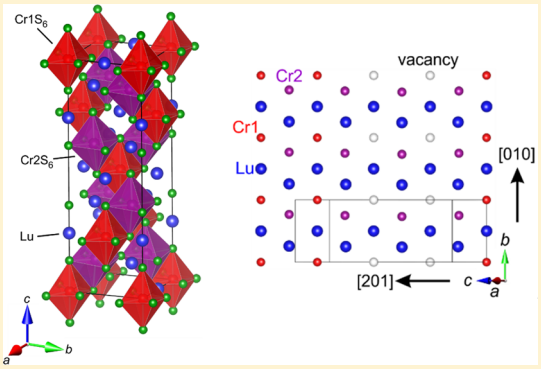

1. INTRODUCTION

Ternary sulfides R_2MS_4 of trivalent rare-earth metal R and divalent metal M show a variety of crystal structures. The reported structures of these sulfides are grouped into several three-dimensional structure types, i.e., the spinel type ($Fd\bar{3}m$),[1−7] the Th_3P_4 type ($I\bar{4}3m$),[5,6,8−11] the olivine type ($Pnma$),[5,6,12] the Yb_3S_4 type ($Pnma$),[5] the $CaFe_2O_4$ type ($Pnma$),[5] the Y_2MnS_4 type ($Cmcm$ or $Cmc2_1$),[1,5,6,13] and so on. The relative stability of these structures is determined by the ionic sizes of the R and M atoms.[5]

For transition metals except Cr, almost of all of the R_2MS_4 phases crystallize in the spinel-, olivine-, and Y_2MnS_4-type structures. The spinel- and olivine-type structures consist of cubic closest packing (CCP) and hexagonal closest packing (HCP) of S atoms, respectively.[1−7,12] In both structures, the R and M atoms occupy the octahedral and tetrahedral holes, respectively. In the Y_2MnS_4-type structures, the R atoms adopt two different coordination environments of 6-coordinated octahedral sites and 7-coordinated polyhedral sites, and the M atoms randomly share the octahedral sites with the R atoms.[1,5,6,13]

For divalent Cr with a high-spin $3d^4$ electronic configuration, the Jahn–Teller effect often plays an important role in structural stabilization and electrical, magnetic, and optical behavior. All of the reported compounds in the chromium systems R_2CrS_4 (R = Ho–Yb, Y) have the Er_2CrS_4-type structure.[6,14−17] The Er_2CrS_4-type structure is very similar to the Y_2MnS_4-type structure, but there exist two long and four short Cr–S bond lengths in the octahedral environment. Because Jahn–Teller ordering prevents cation disordering, the R and Cr atoms occupy independent crystallographic sites. The CrS_6 octahedra share corners and edges, forming a three-dimensional structure. In our previous studies, Y_2CrS_4 showed a long-range antiferromagnetic (AFM) ordering of divalent Cr at 65 K, and its collinear magnetic structure was determined.[17] On the other hand, as far as we know, the description of Lu_2CrS_4 has not been reported yet.

In this work, we succeeded in the synthesis of a new rare-earth chromium sulfide, Lu_2CrS_4. This compound was found to crystallize in a novel CCP structure of S atom, in which both of the Lu and Cr atoms occupy the octahedral holes, forming the rock-salt-type superstructure with Jahn–Teller distortion. We will report the synthesis, crystal structure, and electrical and magnetic properties of Lu_2CrS_4.

Received: July 6, 2015
Published: September 29, 2015

DOI: 10.1021/acs.inorgchem.5b01511
Inorg. Chem. 2015, 54, 9802–9809

2. EXPERIMENTAL SECTION

Powder samples of Lu_2CrS_4 were synthesized by solid-state reactions of CrS with Lu_2S_3. Lutetium sesquesulfide (Lu_2S_3) was prepared by heating Lu_2O_3 on a silica boat at 1150 °C in a flow of the mixed gas of CS_2 and N_2, which was obtained by bubbling N_2 gas through liquid CS_2 at room temperature. Chromium monosulfide (CrS) was prepared by heating a mixture of Cr and S at 1000 °C in an evacuated silica tube (see the Supporting Information). The starting materials were stoichiometrically mixed together and sealed in an evacuated carbon-coated silica tube, and the tube was heated at 1300 °C for 24 h.

Powder X-ray diffraction (XRD) patterns were measured with Cu Kα radiation on a RINT2200 diffractometer (Rigaku) equipped with a graphite monochromator. The crystal structure was determined using *EXPO2004*[18] and refined with the program *RIETAN-FP*.[19] The crystal structures were visualized with the program *VESTA*.[20] Powder neutron diffraction (ND) measurements were performed on the Kinken powder diffractometer for high-efficiency and high-resolution measurements of the Institute for Materials Research at Tohoku University,[21] which was installed at the JRR-3 M Reactor of the Japan Atomic Energy Agency, Tokai, Japan.The crystal and magnetic structures were determined by the Rietveld method using the *FullProf* program.[22]

The temperature dependence of the electrical conductivity was measured by a direct-current (dc) four-probe method in the temperature range between 300 and 400 K. The bar-shaped samples for the resistivity measurements were sintered at 1300 °C for 12 h in an evacuated carbon-coated silica tube. The relative density of the sintered sample was 75.5%. Gold wires (0.030 mm) were used to connect the sample to the stage with contacts made using silver epoxy, while soldered contacts connected the stage to external cables leading to the Keithley 2001 digital multimeter or the ADCMT 8252 electrometer. A dc two-probe method was used in the temperature range between 260 and 350 K. The ohmic contacts were confirmed by the current−voltage characteristics at room temperature.

The magnetic susceptibilities were measured under an applied field of 0.1 T in the temperature range between 4.5 and 300 K by using a SQUID magnetometer (Quantum Design, MPMS-5S). Specific heat measurement was carried out using a relaxation technique supplied by the commercial specific heat measurement system (Quantum Design, PPMS) in the temperature range from 1.8 to 300 K. The sample in the form of a pellet was mounted on an alumina plate with apiezon for good thermal contact. UV−vis diffuse-reflectance spectra were measured with a V-570 instrument (JASCO).

Calculations of the electronic structure and density of states (DOS) were performed using the *WIEN2k* program package.[23] This program employs the full-potential linearized augmented plane wave + local orbitals method based on density functional theory. We used the generalized gradient approximation (GGA) + Hubbard *U* parameter for the Cr 3d electrons. In the calculation, the convergence parameter was set to $R_{MT}k_{max}$ = 7.0, and the muffin-tin (MT) spheres are R_{MT}(Lu) = 2.50 bohr, R_{MT}(Cr) = 2.44 bohr, and R_{MT}(S) = 2.10 bohr. We used 6 × 6 × 2 meshes, which generated 36 *k* points in the first Brillouin zone.

3. RESULTS AND DISCUSSION

3.1. Crystal Structure. Figure 1 shows the XRD pattern of Lu_2CrS_4 at room temperature. This pattern is not similar to any of the known patterns of ternary sulfides including Lu_2MnS_4 with the spinel structure,[1−7] although the divalent ionic radii of Mn and Cr with high-spin states are very close (Mn^{2+}, 0.97 Å; Cr^{2+}, 0.94 Å).[24] The difference in the XRD patterns (i.e., crystal structures) between Lu_2MnS_4 and Lu_2CrS_4 is caused by Jahn−Teller distortion of divalent Cr, as will be described later.

The peaks in the XRD pattern were indexed using both the program *JADE*[25] and the N-Treor algorithm implemented in *EXPO2004*. The space group was determined to be a tetragonal system $I4_1md$ (No. 109) or $I\bar{4}2d$ (No. 122) with $a \sim 7.463$ Å and $c \sim 22.628$ Å based on the unit-cell dimensions and

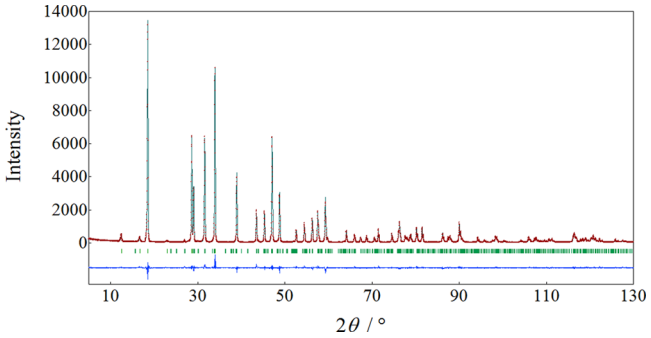

Figure 1. Powder XRD pattern fitting for Lu_2CrS_4. The calculated and observed patterns are shown by the top solid line and cross markers, respectively. The vertical marks in the middle show positions calculated for Bragg reflections. The lower trace is a plot of the difference between the calculated and observed intensities.

systematic extinctions. Because the density of the Lu_2CrS_4 powder was determined to be 5.5(2) g cm^{-3} using a pycnometer, the number of formula units in a unit cell, *Z*, was estimated to be 8. From these data, the crystal structure was solved by direct methods using *EXPO2004*. Although $I4_1md$ (No. 109) and $I\bar{4}2d$ (No. 122) have the same systematic-absence conditions, the structure cannot be solved by the space group $I4_1md$ (No. 109). Then, it was determined that the Lu atoms occupy the 8d and 8c sites, the Cr atoms occupy the 4a and 8d sites, and the S atoms occupy two 8c sites and one 16e site of the space group $I\bar{4}2d$ (No. 122). The structure refinement using the program *RIETAN-FP* was converged to R_{wp} = 8.81% and *S* = 1.29, and the lattice parameters were determined to be *a* = 7.46373(3) Å and *c* = 22.6338(2) Å. When the Cr atoms occupy all of the 4a and 8d sites, the molar ratio of Lu/Cr/S becomes 4:3:8. Thus, the occupancies of the Cr 4a and 8d sites were also refined, and the refined results show that the Cr atoms occupy fully the 4a site and just half of the 8d site within the error range. However, there is a strong correlation between a site occupancy and an atomic displacement parameter. Finally, the site occupancies of the Cr 4a and 8d sites were fixed to 1.0 and 0.5, respectively, and just the atomic displacement parameters of both sites were refined. The final refined results are shown in Table 1 and Figure 1.

Figure 2 shows the crystal structure of Lu_2CrS_4. The Cr1 and Cr2 atoms are 6-coordinated by S atoms, forming CrS_6 octahedra. The $Cr1S_6$ octahedra edge-share to $Cr2S_6$ octahedra. The $Cr2S_6$ octahedra corner-share to each other in directions perpendicular to the *c* axis. The S atoms form a slightly distorted CCP arrangement parallel to {102}, as shown in Figure 3a. It is well-known that the crystal structure is called a rock salt (NaCl)-type structure if one kind of cationic atom completely occupies the octahedral holes in the CCP arrangement. In the case of Lu_2CrS_4, the Lu and Cr atoms fill $^1/_2$ and $^1/_4$ of their octahedral holes, respectively and orderly, and the rest holes remain as vacancies occupying the 4b site at ($^1/_2$, $^1/_2$, 0) and half of the 8d site for Cr2. Figure 3b shows a cationic atom arrangement between CCP sulfur layers. The Lu and Cr (or vacancy labeled as □) atoms arrange alternately in the sequence Lu2Cr1Lu2Cr1, Lu1Cr2Lu1Cr2, and Lu2□Lu2□ along ⟨100⟩ but order successively in the sequence Lu1Lu1Lu1Lu1, Lu2Lu2Lu2Lu2, Cr1□□Cr1 (or Cr1□Cr1□), and Cr2Cr2Cr2Cr2 along ⟨201⟩. Consequently, the Cr (or □) and Lu zigzag chains along ⟨201⟩ alternate parallel to ⟨100⟩. In the case of rock-salt-type ionic compounds

DOI: 10.1021/acs.inorgchem.5b01511
Inorg. Chem. 2015, 54, 9802−9809

Table 1. Crystallographic Data for Lu_2CrS_4 at Room Temperature

	space group			$I\bar{4}2d$ (No. 122, setting 1)		
	a/Å			7.46373(3)		
	c/Å			22.6338(2)		
	R_{wp}/%			8.81		
	S			1.29		
atom	site	g	x	y	z	B/Å^2
Lu1	8d	1.0	0.2543(4)	$^1/_4$	$^1/_8$	1.07(6)
Lu2	8c	1.0	0	0	0.25031(9)	1.11(6)
Cr1	4a	1.0	0	0	0	1.6(3)
Cr2	8d	0.5	0.758(3)	$^1/_4$	$^1/_8$	1.0(3)
S1	8c	1.0	0	0	0.3691(5)	0.3(2)
S2	8c	1.0	0	0	0.1302(5)	1.5(2)
S3	16e	1.0	0.2308(13)	0.2194(13)	0.0073(5)	1.07(13)

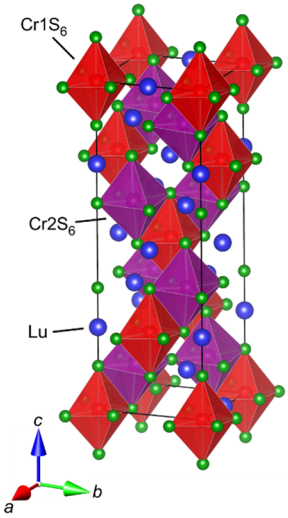

Figure 2. Crystal structure of Lu_2CrS_4.

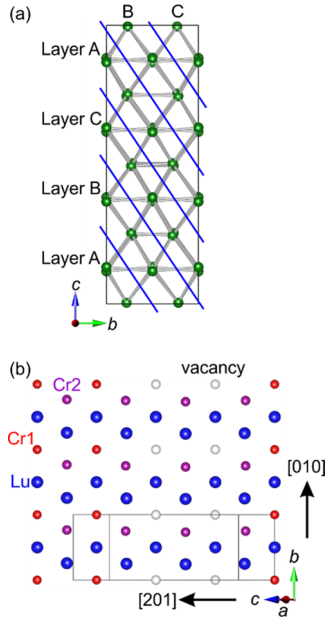

Figure 3. (a) CCP arrangement of S atoms. (b) Cationic atom arrangement adopted by Lu (blue spheres), Cr1 (red spheres), Cr2 (purple spheres), and vacancy (white spheres) between CCP sulfur layers.

containing two or more kinds of cationic atoms, the cations often occupy independent crystallographic sites.[26] As far as we know, no compound with the superstructure of Lu_2CrS_4 exists. However, β-$NaMnO_2$ and β-Li_2CuZrO_4 were reported to have similar cation arrangements consisting of zigzag chains.[26−28] It is interesting to note that the superstructures of both compounds include Jahn−Teller distortions caused by the trivalent Mn $3d^4$ and divalent Cu $3d^9$ electronic configurations, as is the case with Lu_2CrS_4 containing divalent Cr $3d^4$. The Er_2CrS_4-type structure is stable for R_2CrS_4 (R = Ho−Tm) with trivalent lanthanides but unstable for Yb_2CrS_4 because of the partially divalent Yb.[15] Lu is also extremely stable in the trivalent state, but Lu_2CrS_4 does not have a Er_2CrS_4-type structure. From these results, the difference in the crystal structure between Tm_2CrS_4 and Lu_2CrS_4 is thought to be just the difference between both the lanthanide ionic radii, although the trivalent ionic radii of Tm and Lu are very close (Tm^{3+}, 1.02 Å; Lu^{3+}, 1.00 Å).[24]

Bond lengths between Cr and S calculated from the refined data are shown in Figure 4 and Table 2. Two bonds along the c

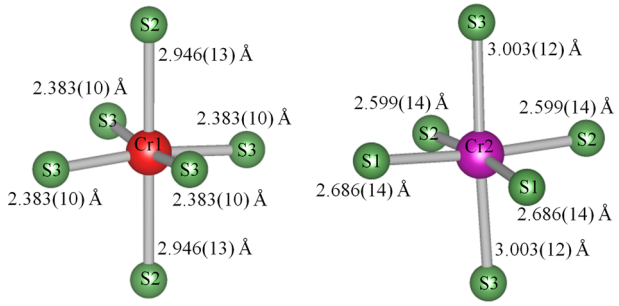

Figure 4. Coordination environments for CrS_6 octahedra.

Table 2. Selected Bond Distances of Lu_2CrS_4

bond	distance (Å)	bond	distance (Å)
Lu1−S1	2.620(3) (×2)	Cr1−S2	2.946(13) (×2)
Lu1−S2	2.664(3) (×2)	Cr1−S3	2.383(10) (×4)
Lu1−S3	2.680(12) (×2)		
Lu2−S1	2.689(10) (×1)	Cr2−S1	2.686(14) (×2)
Lu2−S2	2.720(13) (×1)	Cr2−S2	2.599(14) (×2)
Lu2−S3	2.596(10) (×2)	Cr2−S3	3.003(12) (×2)
Lu2−S3	2.718(10) (×2)		

DOI: 10.1021/acs.inorgchem.5b01511
Inorg. Chem. 2015, 54, 9802−9809

axis for each Cr are obviously longer than the other four bonds, which indicates that the CrS_6 octahedra are distorted because of the Jahn−Teller effect of divalent Cr with the high-spin $3d^4$ electronic configuration, like Er_2CrS_4 and Y_2CrS_4. It is assumed that the difference in the bond lengths is mainly due to the deficiency in the Cr2 8d site, as described in the section about the bond valence sum (BVS). The schematic diagram of the orbital splitting is shown in the Supporting Information. Jahn−Teller distortion of the orbital configurations will be described exactly in the section 3.5. Although a decrease in the distortion can induce a structural phase transition, the transition is not observed below room temperature by the heat capacity (see section 3.4) and ND (see section 3.5) measurements. At higher temperature, the transition may occur as a result of a decrease in the distortion. The Lu−S bond lengths are also shown in Table 2. The BVS method was applied to estimate the valence of Lu using $r_0(Lu^{3+}-S^{2-})$ = 2.414 Å.[29] The BVSs for Lu1 and Lu2 were calculated to be +3.14 and +3.02, respectively, indicating that Lu is in the trivalent state. When the valence of Lu is trivalent, that of Cr is expected to be divalent by considering the overall electroneutrality principle of Lu_2CrS_4. Using $r_0(Cr^{2+}-S^{2-})$ = 2.18 Å,[30] the bond valences for Cr1 and Cr2 were calculated to be +2.56 and +1.37, respectively, showing large deviations between the prediction (+2) and experiments. For the Er_2CrS_4-type structure with no Cr deficiency, the valences of Cr for the Y_2CrS_4 and Er_2CrS_4 phases were calculated to be ca. +2. On the other hand, although Cr2 deficiencies exist in the Lu_2CrS_4 structure, the valence estimations for Cr1 and Cr2 were obtained from the average structure and did not take into account structural relaxation around the Cr2 deficiencies. The local displacements of S atoms presumably lead to overestimation of the valence of Cr1 and to underestimation of the valence of Cr2. The detail discussion of the BVS method should need investigations of the local Cr−S coordination environments. The valence of Cr would be considered the divalent state, as described in the following sections.

3.2. Electrical Conductivity. The electrical resistivity (ρ) for Lu_2CrS_4 was ~7 × 10^7 Ω m at room temperature. The resistivity was measured in the temperature range between 260 and 400 K, and its Arrhenius plot is represented in Figure 5. The resistivity increases with decreasing temperature up to ~2 × 10^8 Ω m at 260 K and shows thermally activated semiconducting (insulating) behavior. However, the temperature dependence does not follow the Arrhenius plot (log $\rho \propto T^{-1}$). The log $\rho - T^{-1/d+1}$ curve (d = number of dimensions) for a Mott variable-range-hopping (VRH) conductor with localized carriers[31] was also examined, but we could not find the most suitable model. As shown in the inset of Figure 5, the $\rho - T^{-1/4}$ plot for three-dimensional VRH is not a linear curve, and the $\rho - T^{-1/3}$ and $\rho - T^{-1/2}$ plots were more bent than the $\rho - T^{-1/4}$ curve, indicating that the temperature dependence of resistivity does not follow the VRH model. Furthermore, the resistivity is high at room temperature as the Cr^{2+} compounds. There is a possibility that the peculiar temperature dependence and high resistivities result from the disappearance of conducting pathways because of the Cr2 site deficiency. It is an obvious fact that this thermally activated behavior of the electrical conductivity shows the localization of $3d^4$ electrons of divalent Cr at their sites.

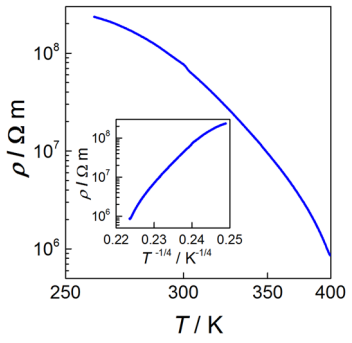

Figure 5. Temperature dependence of the electrical resistivity (ρ). The inset shows the plot of ρ as a function of $T^{-1/4}$ for three-dimensional VRH.

3.3. Magnetic Susceptibility. The magnetic susceptibilities for Lu_2CrS_4 were measured in the temperature range between 4.5 and 300 K. Figure 6 and its inset show the temperature dependence of the magnetic susceptibilities (χ) and inverse magnetic susceptibilities (χ^{-1}), respectively. A drop due to long-range AFM ordering was observed at 55 K, and the absence of divergence between the zero-field-cooled (ZFC) and field-cooled (FC) magnetic susceptibilities indicates that the Cr^{2+} ions are in an AFM state without any weak ferromagnetic properties below 55 K. The peak shape of the anomaly is broad in the temperature range between 60 and 100 K, suggesting the existence of short-range magnetic ordering. The inverse susceptibility obeys the Curie−Weiss law above 150 K. The effective magnetic moment (μ_{eff}) was determined to be 4.93(1) μ_B from the Curie−Weiss fitting. The theoretical effective magnetic moments of Cr^{2+} $3d^4$ with the high-spin state (S = 2) and low-spin state (S = 1) are 4.90 and 2.83 μ_B, respectively. A good agreement between the experimental and theoretical values of S = 2 reveals that the Cr^{2+} ion is in the high-spin state. The Weiss constant was determined to be a large negative value of −142.6(9) K, indicating the existence of AFM interactions between the Cr^{2+} ions.

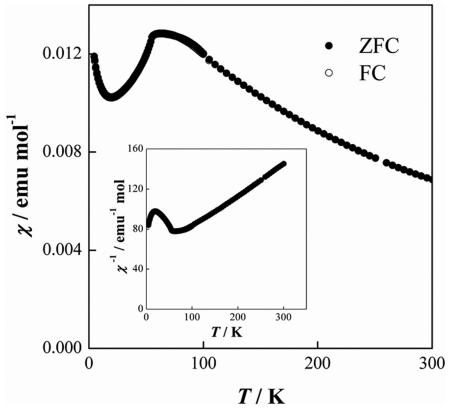

Figure 6. Magnetic susceptibility versus temperature for Lu_2CrS_4. The inset shows the inverse magnetic susceptibilities as a function of the temperature.

3.4. Specific Heat. We measured the specific heat (C_p) of Lu_2CrS_4 and plotted the temperature dependence of C_p in Figure 7a. A λ-type anomaly is observed at 54.5 K, so it is corresponding to the long-range AFM ordering of the Cr^{2+} moments observed in the magnetic measurements (Figure 6). In order to estimate the magnetic contribution (C_{mag}) to C_p, we need to subtract the lattice contribution (C_{lat}) and the

DOI: 10.1021/acs.inorgchem.5b01511
Inorg. Chem. 2015, 54, 9802−9809

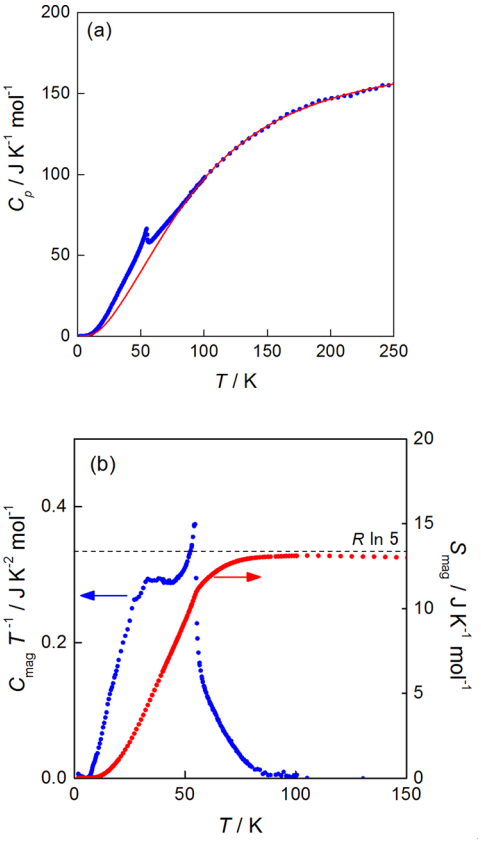

Figure 7. (a) Temperature dependence of the specific heat (C_p) for Lu_2CrS_4. The red solid line is a fit of the lattice contribution to the specific heat according to the Debye and Einstein models as described in the text. (b) Blue and red circle symbols representing the residual specific heat ($C_p - C_{lat}$)/T and the corresponding entropy S_{mag}, respectively.

electronic contribution ($C_e \sim 0$ J mol^{-1} K^{-1} for insulators) from the total C_p. The C_{lat} data were fitted to the measured C_p data between 100 and 250 K using a linear combination of the Debye and Einstein models. The analytical formula was

$$C(T) = n_D \times 9N_A k_B \left(\frac{T}{T_D}\right)^3 \int_0^{T_D/T} \frac{x^4 e^x}{(e^x - 1)^2}\, dx + n_{E1} \times 3N_A k_B \left(\frac{T_{E1}}{T}\right)^2 \frac{e^{T_{E1}/T}}{(e^{T_{E1}/T} - 1)^2} + n_{E2} \times 3N_A k_B \left(\frac{T_{E2}}{T}\right)^2 \frac{e^{T_{E2}/T}}{(e^{T_{E2}/T} - 1)^2}$$

where N_A is Avogadro's constant, k_B is Boltzmann's constant, T_D is the Debye temperature, and T_E is the Einstein temperature. The sum of the scale factors n_D, n_{E1}, and n_{E2} was restricted to the number of atoms per Lu_2CrS_4 chemical formula: $n_D + n_{E1} + n_{E2} = 7$. We adopted the model using one T_D and two T_E because there was a disagreement between the measured C_p data and the C_{lat} data fitted by the simple model using one T_D and one T_E at high temperatures. The fit to the data yielded T_D of 170 K, T_{E1} of 254 K, T_{E2} of 408 K, n_D of 1.95, n_{E1} of 2.39, and n_{E2} of 2.67, and this fitting result is also plotted in Figure 7a.

The temperature dependences of C_{mag}/T [$=(C_p - C_{lat})/T$] and the magnetic entropy S_{mag} ($=\int_0^T (C_{mag}/T')\, dT'$) below 150 K are shown in Figure 7b. The high-temperature tail of the magnetic specific heat above 55 K corresponds to the broad anomaly in the temperature range between 55 and 100 K in the $\chi - T$ curve (Figure 6), suggesting the existence of short-range magnetic ordering due to frustration magnetic interactions as described later. From the $S_{mag} - T$ curve, the S_{mag} change due to the magnetic ordering of the Cr^{2+} moments at 100 K is estimated to be 13.1 J mol^{-1} K^{-1}. This value of S_{mag} is in good agreement with R ln 5 (=13.4 J mol^{-1} K^{-1}) of the theoretical value for the Cr^{2+} ion with $S = 2$.

3.5. Electronic Structure. Figure 8 shows the UV–vis diffuse-reflectance spectrum of Lu_2CrS_4. The absorption

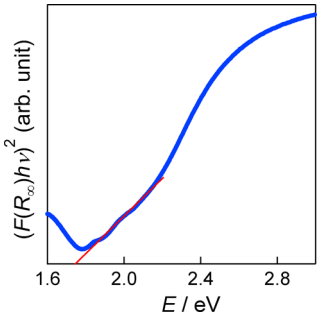

Figure 8. Diffuse-reflectance spectrum of Lu_2CrS_4. The Tauc plot is shown.

coefficients were calculated from the reflectance data with the Kubelka–Munk function.[32] The energy of the optical band gap was determined to be 1.75 eV from the Tauc plot.[33]

Figure 9a displays the total and partial DOS of total electrons of Lu, Cr1, Cr2, and S for Lu_2CrS_4 obtained from the GGA + U

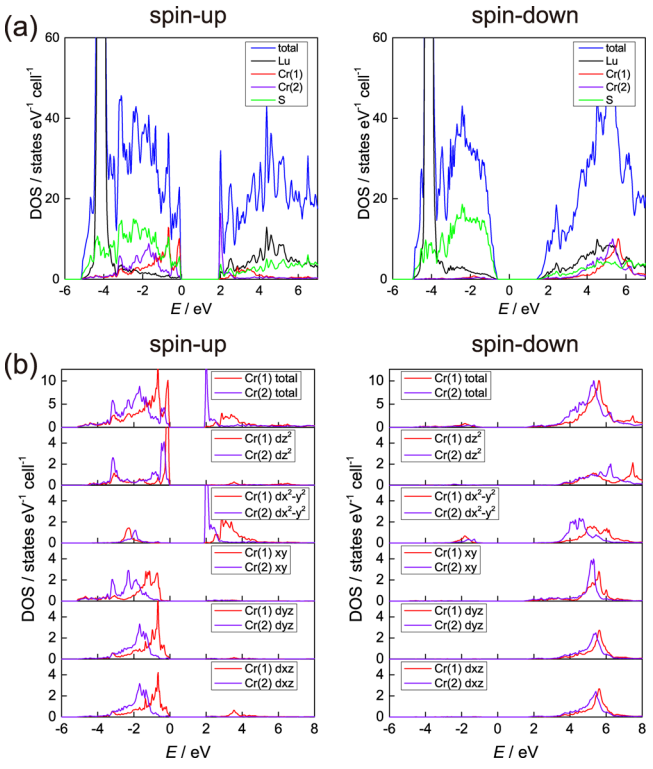

Figure 9. (a) Total and partial DOS of total electrons of Lu, Cr1, Cr2, and S for Lu_2CrS_4 (GGA + U with $U = 5.0$ eV). (b) Partial DOS of the Cr 3d orbitals. The zero energy is placed at the highest occupied state.

DOI: 10.1021/acs.inorgchem.5b01511
Inorg. Chem. 2015, 54, 9802–9809

calculations. In this calculation, the Cr deficiency was considered by removing half of the Cr2 atoms at the 8d site in a 2 × 2 × 1 supercell. The values of U for Hubbard-like effective potentials of Cr1 and Cr2 were set to be 5.0 eV. In Figure 9a, the occupied and unoccupied bands form a band gap of ∼1.5 eV around the Fermi level and are consistent with the result of the UV−vis spectra. The results from the GGA + U calculations demonstrate that the Cr ions are in the divalent state with the high-spin configuration and have the magnetic moments of 3.37 μ_B per Cr1 atom and 3.45 μ_B per Cr2 atom. Figure 9b shows the partial DOS of the Cr1 and Cr2 3d orbitals. The energy levels of the unoccupied orbitals ($d_{x^2-y^2}$) for the Cr spin-up states and all of the Cr spin-down orbitals are located at 2−8 eV, which indicates that the spin-up $d_{x^2-y^2}$ states correspond to one e_g hole for the spin-up Cr^{2+} states. On the other hand, the occupied spin-up $d_{3r^2-z^2}$ states are delocalized over all of the S p bands and split up into two peaks just below E_F and at around −3 eV, forming a bonding/antibonding gap due to strong Cr $d_{3r^2-z^2}$−S p_z σ bondings. These DOS for the spin-up $d_{3r^2-z^2}$ and $d_{x^2-y^2}$ states reveal that the e_g bands of the Cr 3d electrons split into the occupied and unoccupied states due to Jahn−Teller distortion for the $Cr1S_6$ and $Cr2S_6$ octahedra and suggest that the superexchange interactions via the Cr $d_{3r^2-z^2}$−S p_z−Cr $d_{3r^2-z^2}$ and/or Cr $d_{3r^2-z^2}$−S p_z−S p_z−Cr $d_{3r^2-z^2}$ paths play a key role in AFM ordering.

3.6. Magnetic Structure. Figure 10 shows the ND profiles of Lu_2CrS_4 at 10, 80, and 300 K using a wavelength of 1.8449 Å. Only the nuclear Bragg reflections are observed at 80 and 300 K, and the crystal structure was refined by the Rietveld method. The obtained parameters are in good agreement with those obtained from the XRD measurement. The structural parameters at 80 K are summarized in Table S1 in the Supporting Information.

In the ND profile at 10 K, several additional Bragg reflections appear. The temperature dependence of the magnetic susceptibility of Lu_2CrS_4 has a maximum around 60 K, and the specific heat shows long-range AFM ordering at 55 K. It is considered that these additional Bragg reflections at 10 K are attributable to magnetic scatterings of long-range AFM ordering of the Cr ions. The magnetic Bragg reflections are indexed to the ($^1/_2$, $^1/_2$, l) and ($^1/_2$, $^3/_2$, l) planes, which indicates that the propagation vector $\mathbf{k}$ in the magnetic ordered state is $\mathbf{k}$ = ($^1/_2$, $^1/_2$, 0).

The symmetry and directions of the magnetic moments compatible with the crystal symmetry ($I\bar{4}2d$) were obtained using the program *SARAh*.[34] The decompositions of magnetic representations are $\Gamma_{mag} = 6\Gamma_1^{(2)}$ for both the 4a (Cr1) and 8d (Cr2) sites. The constraint from the Landau theory requires six possible magnetic structures for each Cr ion. In general, in the case of the second-order magnetic phase transition, one magnetic structure model should be obtained from the combination of 12 possible directions of the magnetic moments $\Gamma_{mag} = 6\Gamma_1^{(2)}(Cr1) + 6\Gamma_1^{(2)}(Cr2)$, but the magnetic peak profile fittings using the simple model did not agree with the observed magnetic reflections.

Then, we attempted refinement using magnetic structures with two sets of models constrained by the Landau theory. The best results of the refinements indicated that most of the components of the magnetic moments were the z components as the following model. The Cr1 site has two magnetic independent sites, and the Cr2 site has four magnetic independent sites. The positive and negative signs of the z components of these independent sites are listed in Table 3, and the magnetic structures in the nuclear unit cell are illustrated in Figure 11. There exist 16 90° Cr1−S−Cr2 (J_1) superexchange interactions and 4 180° Cr2−S−Cr2 (J_2) superexchange interactions in the nuclear unit cell. For the proposed model, because of quenching of the magnetic moments of four Cr2 sites in the magnetic structure, eight J_1 paths and all J_2 paths vanish. Consequently, there remain eight J_1 paths between the nearest-neighbor magnetic moments, and two arrays are parallel and the other six arrays are antiparallel. According to the Goodenough−Kanamori rules, because the

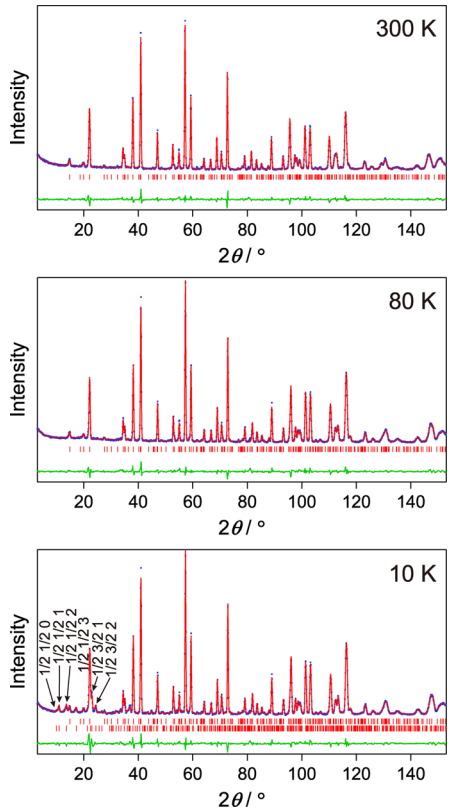

Figure 10. ND profiles for Lu_2CrS_4 at 10, 80, and 300 K. The calculated and observed diffraction profiles are shown as the top solid line and the markers, respectively. The trace at the bottom is a plot of the difference between the calculated and observed intensities. For the profiles at 80 and 300 K, the set of vertical markers in the middle show positions calculated from nuclear Bragg reflections. For the profile at 10 K, the upper set of vertical markers in the middle show positions calculated from nuclear Bragg reflections. The lower set of vertical markers in the middle show positions calculated from magnetic Bragg reflections.

Table 3. Possible Magnetic Structure Model for Lu_2CrS_4 at 10 K

atom	site	g	x	y	z	m_Z
Cr1	4a	1.0	0	0	0	+
		1.0	0	$^1/_2$	$^1/_4$	+
Cr2	8d	0.5	α^a	$^1/_4$	$^1/_8$	0
		0.5	$-\alpha^a$	$^3/_4$	$^1/_8$	−
		0.5	$^1/_4$	$-\alpha^a$	$^7/_8$	−
		0.5	$^3/_4$	α^a	$^7/_8$	0

$^a\alpha \sim 0.76$.

DOI: 10.1021/acs.inorgchem.5b01511
Inorg. Chem. 2015, 54, 9802−9809

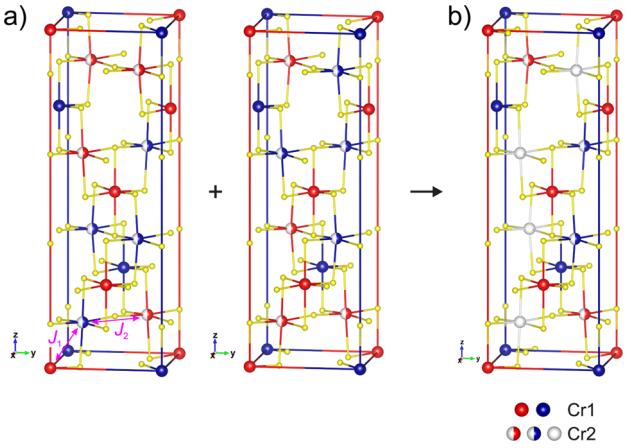

Figure 11. Possible magnetic structure models of the Cr moments: (a) magnetic structure models constrained by the Landau theory; (b) model of their combination. The z components of the magnetic moments of blue and red spheres are antiparallel to each other. The white Cr spheres mean quenching of the contribution to the magnetic structure factors because of the offset between the up and down moments.

180° and 90° superexchange interactions between high-spin d^4 electrons are predicted to be quasistatic ferromagnetic and quasistatic AFM, respectively,[35] the magnetic interactions between the Cr^{2+} ions are expected to be competitive. In addition to the deficiency of the Cr2 sites, these competitive interactions are reflected in the complicated magnetic structure. Unfortunately, even refinements using the combination of two sets of magnetic structure models could not achieve a good agreement between the calculated and observed magnetic Bragg reflections [R_B(nuc.) = 3.1%; R_B(mag.) = 11.0%]. Furthermore, the obtained magnetic moment $|m|$ = 4.0(1) μ_B agrees with the theoretical value (4 μ_B) but is larger than the values (3.3−3.5 μ_B) observed for other high-spin d^4 compounds.[17] Because it is too difficult to solve the magnetic structure with more than two models, we propose the magnetic structure in Figure 11b as a basic structure model.

4. CONCLUSIONS

We succeeded in synthesizing a new compound, Lu_2CrS_4, and determining the new crystal structure with a tetragonal system, with a = 7.46373(2) Å, c = 22.6338(2) Å, and space group $I\bar{4}2d$ (No. 122). The $Cr1S_6$ octahedra are edge-shared to $Cr2S_6$ octahedra, and the $Cr2S_6$ octahedra are corner-shared to each other in directions perpendicular to the c axis, which indicates a rock-salt superstructure with new cation (vacancy) arrangements.

The electrical resistivity was ∼7 × 10^7 Ω m at room temperature and increases with decreasing temperature, showing thermally activated semiconducting behavior. An AFM anomaly was found at 54.5 K from the magnetic susceptibility and specific heat measurements, and the Cr ions were in the divalent high-spin state. Short-range magnetic ordering was also observed above the anomalous temperature because of the deficiency of the Cr2 site. From the ND profile at 10 K, the propagation vector $\mathbf{k}$ in the magnetically ordered state was determined to be $\mathbf{k}$ = ($^1/_2$, $^1/_2$, 0). The z component of the magnetic moment was dominant, and the basic magnetic structure could be expressed as the combination of two models constrained by the Landau theory. The optical band-gap energy was determined to be 1.75 eV from the Tauc plot. The optical band-gap energy, divalent high-spin state of Cr, and Jahn−Teller distortion were supported by the calculated results of the DOS.

■ ASSOCIATED CONTENT

Supporting Information

The Supporting Information is available free of charge on the ACS Publications website at DOI: 10.1021/acs.inorgchem.5b01511.

CIF files giving structural data of Lu_2CrS_4 at room temperature (XRD) (CIF)

CIF files giving structural data of Lu_2CrS_4 at 80 K (ND) (CIF)

Synthesis of CrS, level splitting of the 3d orbitals in Jahn−Teller distortion, and crystallographic data at 80 K (PDF)

■ AUTHOR INFORMATION

Corresponding Author

*E-mail: ktez@cc.utsunomiya-u.ac.jp.

Notes

The authors declare no competing financial interest.

■ ACKNOWLEDGMENTS

This work was partially supported by JSPS KAKENHI Grant 19750040.

■ REFERENCES

(1) Patrie, M.; Chevalier, R. *C. R. Seances Acad. Sci., Ser. C: Sci. Chim.* **1966**, *263*, 1061−1064.
(2) Patrie, M.; Flahaut, J.; Domange, L. *C. R. Hebd. Seances Acad. Sci.* **1964**, *258*, 2585−2586.
(3) Fujii, H.; Okamoto, T.; Kamigaichi, T. *J. Phys. Soc. Jpn.* **1972**, *32*, 1432−1432.
(4) Tomas, A.; Tien, V.; Guittard, M.; Flahaut, J.; Guymont, M. *Mater. Res. Bull.* **1985**, *20*, 1027−1030.
(5) Lowe-Ma, C. K.; Vanderah, T. A.; Smith, T. E. *J. Solid State Chem.* **1995**, *117*, 363−372.
(6) Mitchell, K.; Ibers, J. A. *Chem. Rev.* **2002**, *102*, 1929−1952.
(7) Barahona, P.; Llanos, J.; Peña, O. *J. Mater. Chem.* **2006**, *16*, 1567−1572.
(8) Ben-Dor, L.; Shilo, I.; Felner, I. *J. Solid State Chem.* **1978**, *24*, 401−404.
(9) Ben-Dor, L.; Shilo, I. *J. Solid State Chem.* **1980**, *35*, 278−285.
(10) Li, P. Y.; Lange, K. G.; Andratschke, M.; Range, K. J. *Z. Kristallogr.* **1996**, *211*, 814−814.
(11) Laronze, H.; Demourgues, A.; Tressaud, A.; Lozano, L.; Grannec, J.; Guillen, F.; Macaudière, P.; Maestro, P. *J. Alloys Compd.* **1998**, *275-277*, 113−117.
(12) Rodier, N.; Tien, V. *C. R. Seances Acad. Sci. Ser. C* **1977**, *284*, 909−911.
(13) Patrie, M.; Flahaut, J. *C. R. Seances Acad. Sci. Ser. C* **1967**, *264*, 395.
(14) Tomas, A.; Chevalier, R.; Laruelle, P.; Bachet, B. *Acta Crystallogr., Sect. B: Struct. Crystallogr. Cryst. Chem.* **1976**, *32*, 3287−3289.
(15) Tomas, A.; Guittard, M.; Chevalier, R.; Flahaut, J. *C. R. Seances Acad. Sci., Ser. C: Sci. Chim.* **1976**, *282*, 587−589.
(16) Vaqueiro, P.; Szkoda, I.; Sanchez, R. D.; Powell, A. V. *Inorg. Chem.* **2009**, *48*, 1284−1292.
(17) Tezuka, K.; Shan, Y. J.; Imoto, H.; Ohoyama, K. *J. Phys. Chem. Solids* **2007**, *68*, 2133−2137.
(18) Altomare, A.; Caliandro, R.; Camalli, M.; Cuocci, C.; Giacovazzo, C.; Moliterni, A. G. G.; Rizzi, R. *J. Appl. Crystallogr.* **2004**, *37*, 1025−1028.

DOI: 10.1021/acs.inorgchem.5b01511
Inorg. Chem. 2015, 54, 9802−9809

(19) Izumi, F.; Momma, K. *Solid State Phenom.* **2007**, *130*, 15−20.
(20) Momma, K.; Izumi, F. *J. Appl. Crystallogr.* **2011**, *44*, 1272−1276.
(21) Ohoyama, K.; Kanouchi, T.; Nemoto, K.; Ohashi, M.; Kajitani, T.; Yamaguchi, Y. *Jpn. J. Appl. Phys.* **1998**, *37*, 3319−3326.
(22) Rodriguez-Carvajal, J. *Phys. B* **1993**, *192*, 55−69.
(23) Blaha, P.; Schwarz, K.; Madsen, G. K. H.; Kvasnicka, D. *User's Guide for WIEN2k: An Augmented Plane Wave Plus Local Orbitals Program for Calculating Crystal*; Vienna University of Technology: Vienna, Austria, 2001; ISBN 3-9501031-1-2.
(24) Shannon, R. D. *Acta Crystallogr., Sect. A: Cryst. Phys., Diffr., Theor. Gen. Crystallogr.* **1976**, *32*, 751−767.
(25) *JADE 6*; Materials Data Inc.: Livermore, CA, 2002.
(26) Mather, G. C.; Dussarrat, C.; Etourneau, J.; West, A. R. *J. Mater. Chem.* **2000**, *10*, 2219−2230.
(27) Parant, J. P.; Olazcuaga, R.; Devalette, M.; Fouassier, C.; Hagenmuller, P. *J. Solid State Chem.* **1971**, *3*, 1−11.
(28) Dussarrat, C.; Mather, G. C.; Caignaert, V.; Domengès, B.; Fletcher, J. G.; West, A. R. *J. Solid State Chem.* **2002**, *166*, 311−319.
(29) Brown, I. D. *Chem. Rev.* **2009**, *109*, 6858−6919.
(30) Brese, N. E.; O'Keeffe, M. *Acta Crystallogr., Sect. B: Struct. Sci.* **1991**, *47*, 192−197.
(31) Mott, N. F. *J. Non-Cryst. Solids* **1968**, *1*, 1−17.
(32) Kubelka, P.; Munk, F. *Z. Techn. Physik* **1931**, *12*, 593−601.
(33) Tauc, J.; Grigorovici, R.; Vancu, A. *Phys. Status Solidi B* **1966**, *15*, 627−637.
(34) Wills, A. S. *Phys. B* **2000**, *276*−*278*, 680−681.
(35) Goodenough, J. B. *Magnetism and Chemical Bond*; Interscience: New York, 1963.

DOI: 10.1021/acs.inorgchem.5b01511
Inorg. Chem. 2015, 54, 9802−9809